Full length article

Massive nanoprecipitation in an Fe-19Ni-xAl maraging steel triggered by the intrinsic heat treatment during laser metal deposition

Philipp Kürnsteiner [a, *], Markus B. Wilms [b], Andreas Weisheit [b], Pere Barriobero-Vila [c], Eric A. Jägle [a], Dierk Raabe [a]

[a] Department Microstructure Physics and Alloy Design, Max-Planck-Institut für Eisenforschung GmbH, Düsseldorf 40237, Germany
[b] Fraunhofer Institute for Laser Technology ILT, Aachen 52074, Germany
[c] Institute of Materials Science and Technology, Vienna University of Technology, Vienna 1040, Austria

ARTICLE INFO

ABSTRACT

Due to the layer-by-layer build-up of additively manufactured parts, the deposited material experiences a cyclic re-heating in the form of a sequence of temperature pulses. In the current work, this "intrinsic heat treatment (IHT)" was exploited to induce the precipitation of NiAl nanoparticles in an Fe-19Ni-xAl (at%) model maraging steel, a system known for rapid clustering. We used Laser Metal Deposition (LMD) to synthesize compositionally graded specimens. This allowed for the efficient screening of effects associated with varying Al contents ranging from 0 to 25 at% and for identifying promising concentrations for further studies. Based on the existence of the desired martensitic matrix, an upper bound for the Al concentration of 15 at% was defined. Owing to the presence of NiAl precipitates as observed by Atom Probe Tomography (APT), a lower bound of 3—5 at% Al was established. Within this concentration window, increasing the Al concentration gave rise to an increase in hardness by 225 HV due to an exceptionally high number density of 10^{25} NiAl precipitates per m^3, as measured by APT. This work demonstrates the possibility of exploiting the IHT of the LMD process for the production of samples that are precipitation strengthened during the additive manufacturing process without need for any further heat treatment.

1. Introduction

Laser Metal Deposition (LMD) (also termed Direct Metal Deposition (DMD) or Laser Engineered Net Shaping (LENS) is a Laser Additive Manufacturing (LAM) process that allows production of small, custom-made parts directly from a Computer Aided Design (CAD) model and metal powders. Through a feeding nozzle, the metallic powder is injected locally into the melt pool created by a focused high power laser beam on the substrate surface. In the melt pool, the powder is completely melted. The resulting, dense parts can present similar or even better mechanical properties than the conventionally produced bulk metal [1—4]. As for each additive manufacturing process, the starting point is a CAD model. The CAD model is sliced into virtual layers of defined thicknesses. These slices of the sample are then sequentially built by the LMD machine, transferring the geometrical information from the CAD model to

the part [3]. Three aspects of the LMD process are particularly important to this study: Firstly, high cooling rates can be achieved during solidification ($\sim 10^2$-10^5 K^{-1} [2,5—7]) due to the small melt pool size and effective heat conduction into the underlying layers and the substrate. Secondly, as the laser passes by a previously deposited material volume during deposition of neighboring tracks and subsequent layers, the material experiences cyclic reheating with gradually decaying temperature. This type of Intrinsic Heat Treatment (IHT) consists of sharp temperature pulses up to temperatures close to the melting point [5,8,9]. Compared to conventional production, LMD-produced parts, therefore, have a rather complex thermal history [10]. Thirdly, LMD as a nozzle-based LAM process, permits tunability of the chemical composition of components even during the manufacturing process by using two or more powder feeders and a powder mixing chamber before the feeding nozzle. This does not only enable production of functionally graded materials (FGMs) [11,12] to obtain different material properties at different positions, but also to quickly iterate materials compositions to identify the optimum ones [13]. Here, we produce

* Corresponding author.
  E-mail address: p.kuernsteiner@mpie.de (P. Kürnsteiner).

samples that are compositionally graded along the build direction of the part.

Maraging steels belong to a class of Advanced High Strength Steels (AHSS) that combine ultra-high strength with good toughness and ductility. They are of great importance in tooling, aerospace and energy industries [14–16]. These beneficial mechanical properties are caused by a martensitic microstructure hardened by a high density of intermetallic precipitates formed upon aging heat treatment [17,18]. Due to their low-carbon content, high-Ni maraging steels are typically relatively soft, with tensile strength values around 1–1.2 GPa and easy to machine in the as-quenched state [19]. Conventional maraging steels are hardened by a variety of intermetallic phases such as NiMn (Θ-phase), NiAl (β'-phase), Ni_3Ti (η-phase), Ni_3Al, Fe_2Mo (Laves-phase), Ni_2AlMn or Ni_2AlTi [14,20]. Specifically, Ti-free maraging steels containing Ni and Al can be strengthened by the precipitation of ordered β'-NiAl phase [21–27] or Ni_3Al precipitates [14,18,28,29]. Due to their low lattice mismatch of 0.14% [26] with the surrounding martensitic matrix, NiAl precipitates are found to have a spherical shape [30] up to a size of about 45 nm diameter when they start to adopt a cuboidal shape. They lose their coherency at rather large sizes of around 150–300 nm and are usually found distributed homogenously throughout the matrix [26,27]. Furthermore, it has been shown that precipitation kinetics can be very fast for Al and Ti. Pereloma et al. [18] found that Ni-Ti Al clusters which formed after only 5 s of ageing at 550 °C lead to a substantial increase in hardness of 200 HV in a Fe-20Ni-1.8Mn-1.5Ti-0.59Al steel. In a later study they showed that this rapid clustering was followed by $(Ni,Fe)_3Ti$ and $(Ni,Fe)_3(Al,Mn)$ precipitation after aging for 60 s at the same temperature [29]. Taillard et al. [26] observed that an Fe-19Cr-4Ni-1.9Al alloy reached peak hardness already after 1 min aging at 923 °C due to precipitation of fine NiAl particles. Both, Al and Ti, are therefore ideal candidates for the production of an in-process precipitation strengthened maraging steels during the cyclic re-heating associated with the IHT. Here, we study the effect of the IHT in a simple model ternary maraging steel. Due to the above mentioned promising features of the NiAl phase, Al was chosen as systematically varied solute element in this study.

Maraging steels are very well suited for LAM due to their low C content (i.e. good weldability). Furthermore, the high cooling rates provided by the LAM process are ideal for producing a fully martensitic microstructure. Additionally, the IHT can be used to trigger precipitation or clustering that would otherwise require imposing an additional heat treatment process step in the conventional production of such alloys [31]. The effectiveness of the IHT on phase transformations has been shown in previous studies on different alloys such as Ti-6Al-4V [32–34], austenitic stainless steels [35], martensitic stainless steels [36] and maraging steels [31]. However, the IHT has not yet been exploited to design new alloys that are specifically tailored to the AM process. It has been proven that maraging steels can be processed by LAM methods (e.g. LMD [37,38], Selective Laser Melting (SLM) [39]) using existing commercial alloys. Since these alloys were developed and optimized for a conventional production process they are usually not necessarily likewise suited to exploit the specific inherent process features and advantages associated with the LAM process. For example, LAM parts made from commercial maraging alloys such as 18Ni-300 need to undergo an aging heat treatment because of the relatively sluggish precipitation of Mo-containing precipitate phases [39]. The aim of the present study is to develop a maraging steel that fully exploits the capabilities of the LMD process such as high cooling rate and IHT to produce a microstructure that is already precipitation strengthened during synthesis in a one step process without the need for further heat treatment. To the best of the author's knowledge no previous attempts have been made to develop such a maraging steel alloy specifically designed for the LAM process. Furthermore, the authors are not aware of any study in which the Al concentration for a maraging steel was varied up to 25 at%.

Here, we present a methodology to efficiently screen different alloy compositions to identify promising regions for further, in-depth studies. Specifically, we vary the Al concentration of a model maraging steel (containing 19 at% Ni and varying Al concentrations) to identify an alloy composition that responds well to the IHT of the LAM process to produce an in-process precipitation strengthened maraging steel. Precipitation reactions occurring during this IHT will be investigated using a combination of different analytical techniques. Atom Probe Tomography (APT), providing chemical information at near-atomic resolution, is an ideal tool for analyzing small clusters and precipitates [40–45]. High energy synchrotron X-Ray diffraction (HEXRD) can provide accurate crystallographic information of the bulk material with high sensitivity — a technique that is perfectly complementary to APT.

2. Materials and methods

2.1. Additive manufacturing

Samples for this study were produced from metal powders using a 5-axis handling system and a fiber coupled diode laser system LDM 3000-60 by Laserline (Laserline GmbH, Mülheim-Kärlich) with a maximum output of 3 kW, a specific wavelength of 976 nm and a beam parameter product of 60 mm*mrad. The optical system consists of a collimation lens (f_c = 65 mm) and a focusing lens (f_f = 195 mm) resulting in a final beam diameter of 1.8 mm. The powder is fed by means of a disc-based feeding system Sulzer Metco Twin 10C (OC Oerlikon AG, Pfäffikon, Switzerland), where the metal powder particles are conveyed by Argon carrier gas. The used powder feeding system is capable of feeding powder material by two independent powder containers simultaneously. Both carrier streams can be combined to a single stream by usage of a Y-piece before entering the 3- way nozzle (Fraunhofer ILT, Aachen, Germany) and finally the melt pool. Argon is used as a shielding gas to prevent the melt pool from oxidation. In order to build graded structures the rotation speed of the discs in both powder containers can be adjusted to acquire the desired mixture of metal particles and consequently of the final composition of each layer of the bulk volume.

Graded bulk samples were produced by using a bidirectional scan strategy, depositing twelve single tracks next to each other with a constant track offset of 900 μm. Twelve layers were deposited in total with a constant height offset of 700 μm. The laser power of 640 W and the deposition speed of 600 mm/min were also kept constant for every layer. The output of the Al feeder is increased after every second layer starting from 0 g per minute in steps of 0,1 g/minute while the Fe-19Ni (at%) is kept at a constant output of 7.2 g/minute in every layer. Using commercially pure Fe and Ni, the Fe-19Ni (at%) alloy was cast into rods of 75 mm diameter that were then atomized by TLS (TLS Technik GmbH & Co., Bitterfeld, Germany) using the crucible free Electrode Induction-melting Gas Atomization (EIGA) process. The particle fraction used was 45–90 μm. The Al powder used was prepared by TLS (TLS Technik GmbH & Co., Bitterfeld, Germany) with a particle fraction of 20–90 μm.

2.2. Analytical methods

Scanning electron microscopy including Energy Dispersive X-Ray Spectroscopy (EDS) and Electron Backscatter Diffraction (EBSD) was performed in a Zeiss 1540XB cross beam Scanning Electron
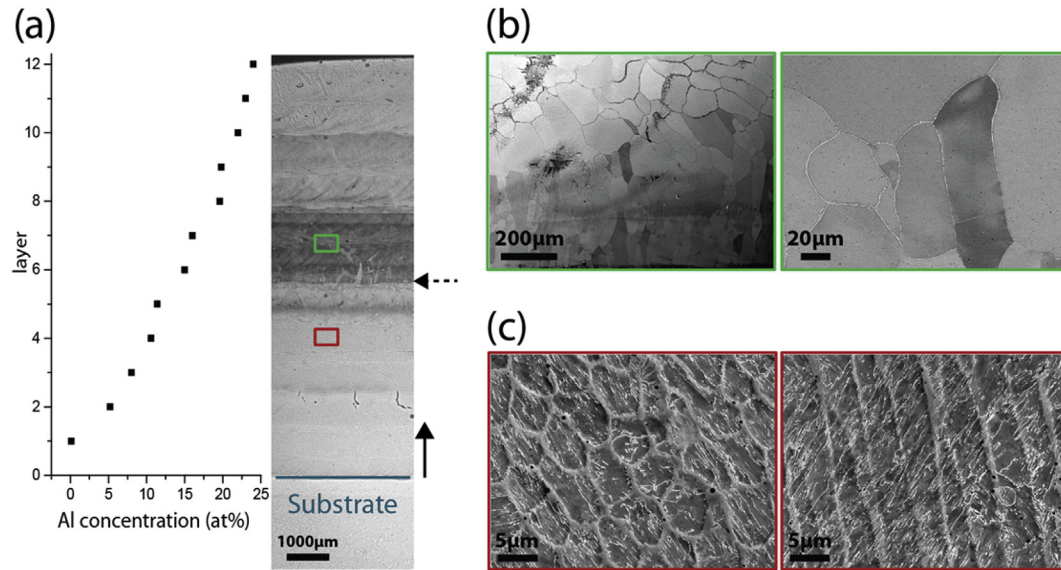
Fig. 1. Overview of the two different regions formed in the graded sample depending on the Al concentration; sample prepared parallel to the build direction (BD, indicated by the solid, vertical arrow) and parallel to the laser scan direction (left to right); (a) Overview of the microstructure as a light optical micrograph plus Al concentration in at% as obtained from SEM-EDS plotted against the layer number; (b) SEM micrograph (backscatter electron contrast) of the microstructure of the coarse grained ferritic region; (c) Two SEM micrographs (secondary electron contrast) of the microstructure of the fine grained martensitic region. Areas with cell/dendrite long axes perpendicular (left) and parallel (right) to the image plane are shown.

Microscope (SEM)-Focused Ion Beam (FIB) setup featuring a GEMINI I Schottky field emission gun electron column. For EDS a TSL Apollo XL Silicon Drift detector featuring a 30 mm^2 detector area and an energy resolution better than 131 eV (measured at the Mn$_{K\alpha}$ Line) was used. EDSD was performed with an EDAX Hikari camera using an acceleration voltage of 15 kV. The TSL OIM Analysis™ software (version 7) was used for EBSD data analysis. Samples were prepared using standard metallographic techniques with a finishing step of 15 min polishing using colloidal silica suspension (OP-S from Stuers ApS, Ballerup, Denmark). For light optical microscopy (LOM) and SEM imaging the samples were additionally etched for 30 s using 5% Nital.

APT samples were prepared by the Standard Lift-Out Process [46] in a FEI Helios NanoLab 600i FIB/SEM dual beam device, equipped with an Omniprobe micromanipulator. Tips were placed on a 6 × 6 silicon microtip coupon and sharpened by applying annular milling patterns at 30 kV acceleration voltage with FIB currents ranging from 0.26 nA for the largest pattern to 46 pA for the smallest one. At the end, a low kV milling at 5 kV acceleration voltage and 40 pA was applied to minimize Ga contaminations at the surface. In this way site specific sample preparation from different layers (i.e. different Al concentrations) of the graded sample were produced. APT experiments were performed in a Cameca LEAP 3000X HR and LEAP 5000 XS at a pressure of less than 10^{-10} mbar in voltage mode using a pulse frequency of 200 kHz and a pulse height of either 15% or 20% of the applied voltage. Temperature and evaporation rate were adjusted in such way to make sure that all Al ions are post ionized and only occur in charge states of Al^{2+} and Al^{3+} but not as Al^{1+} in order to avoid the peak overlap of Al^{1+} with Fe^{2+}. Hence, temperatures in the range of 60–70 K and evaporation rates of 1–3% (every 100th to every 33rd voltage pulse actually triggering an evaporation event) were used. 3D reconstruction was conducted using the commercial software IVAS version 3.6.14. Voxel-based analysis was performed with a spacing of 1 nm and a delocalization of 3 nm.

High energy synchrotron X-ray diffraction (HEXRD) was carried out in transmission mode at the ID22 beamline of the European

Synchrotron Radiation Facility (ESRF, Grenoble, France). A beam energy of 70 keV, a wavelength of 0.177 Å, an exposure time of 2 s, a sample-detector distance of 698.2 mm, a slit size of 500 × 50 μm^2 and a Perkin Elmer XRD 1611 image plate detector were used. A sample of 2 × 2 × 25 mm^3 was cut from the graded sample with the long axis being parallel to the build direction (BD) i.e. the Al concentration varies from 0% to approximately 25% along the long axis. This sample was spun at 300 rpm during acquisition of sequences of complete Debye-Scherrer rings from the bulk of the sample using an image plate detector. Starting from the top (highest Al concentration) the measurements were performed with a step size of 0.5 mm down to the bottom of the sample (0% Al concentration). Instrument parameters of the diffraction setup were obtained using a LaB$_6$ powder standard. Azimuthal integration of the intensity along the Debye-Scherrer rings was performed using the software Fit2d [47,48]. Quantitative phase analysis of the diffraction patterns was carried out by the Rietveld method as implemented in the software Maud [49].

3. Results

Fig. 1(a) shows the Al concentration in the different layers of the graded sample along its build direction. The concentration was obtained via EDS in the SEM. To minimize the influence of any inhomogeneity in the microstructure, instead of spot measurements, rather large areas of 200 × 200 μm were mapped in the middle of each layer and then the entire region of the so obtained map was used for compositional quantification. The results show that the Al concentration varies from 0 at% Al in the bottom layer to approximately 25 at% in the top layer. At around 15 at% Al we observe a sharp transition (indicated via the dashed, horizontal arrow in Fig. 1(a)) from a fine grained martensitic microstructure to a coarse grained ferritic microstructure. SEM images of both microstructures are shown in Fig. 1(b) and (c). The images reveal that martensitic microstructures were only obtained for Al concentrations below 15 at%. This value can thus be defined as the upper bound of an Al concentration range when aiming at synthesizing
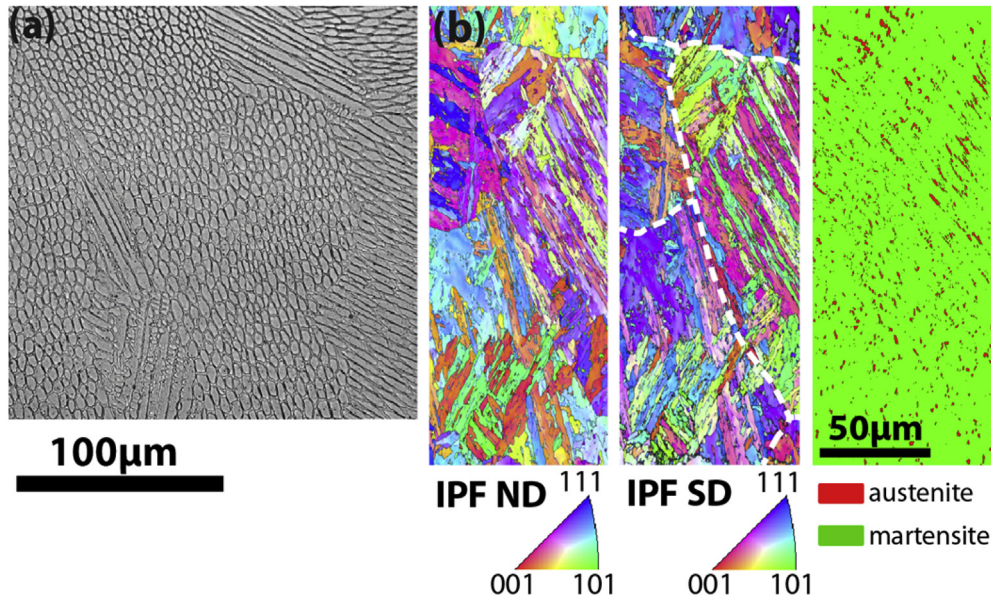
Fig. 2. (a) Light optical micrograph showing the cellular/dendritic solidification structure. (b) Electron Backscatter Diffraction (EBSD) mapping showing the martensitic microstructure by means of Inverse Pole Figures (IPFs) and the spatial distribution of the two phases martensite (green) and austenite (red) in the same area. The two Inverse Pole Figure (IPF) maps are shown with respect to normal direction (ND) and laser scan direction (SD). The white, dashed line on the SD IPF map indicates boundaries between dendrite bundles. For both LOM and EBSD the sample was prepared parallel to the build direction and parallel to the laser scan direction. (For interpretation of the references to colour in this figure legend, the reader is referred to the web version of this article.)

maraging steels with good mechanical properties. This compositional range was thus investigated in more detail.

The microstructure in this region consists of very fine solidification dendrites. Bundles of these dendrites are growing in the same direction as shown in Fig. 2(a). Note that the secondary arm spacing of the dendrites is rather small and in some regions, the solidification structure seems to be almost cellular. These cells appear equiaxed when viewed perpendicular, lath shaped when viewed parallel and elongated, elliptical when viewed at an angle. This fine cellular/dendritic solidification morphology is typical of steels produced by LAM (cf. SLM-produced 18Ni-300 maraging steel [38,39,50], LMD-produced 316 L stainless steel [6]).

The martensitic microstructure is depicted in the Electron Backscatter Diffraction (EBSD) mappings of Fig. 2(b). The two Inverse Pole Figure (IPF) maps are shown with respect to normal direction (ND, normal to sample surface) and laser scan direction (SD, left to the right). The EBSD mapping depicts multiple dendrite bundles. Boundaries between these bundles (all of which are high-angle boundaries) are highlighted in terms of a white, dashed line

on the SD IPF map. The martensite microstructure is superimposed on the dendrite solidification structure with martensite laths crossing multiple dendrites of the same orientation. This interpretation is also supported by the SEM images of Fig. 1(c): fine white lines are crossing multiple dendrite boundaries. The martensite transformation seems to take place independent of the individual dendrites within one bundle. Some austenite islands were also present as can be seen from the phase map of Fig. 2(c). Rejection of solute atoms at the solidifying dendrite boundaries [6,7] (i.e. microsegregation during solidification) leads to an enrichment of Ni and Al in the interdendritic space as revealed in the two EDS maps in Fig. 3. Ni stabilizes the austenite phase, but as the enrichment of the dendrite boundaries is not homogenous (a region of stronger enrichment is indicated by a white circle in Fig. 3), austenite might only occur at certain regions along the dendrite boundaries where the enrichment in Ni is strong enough to stabilize austenite in such alloys [17,51–53]. As can be seen from the Al map of Fig. 3, also few small (100–500 nm) Aluminum oxide particles were found to be present in the microstructure.
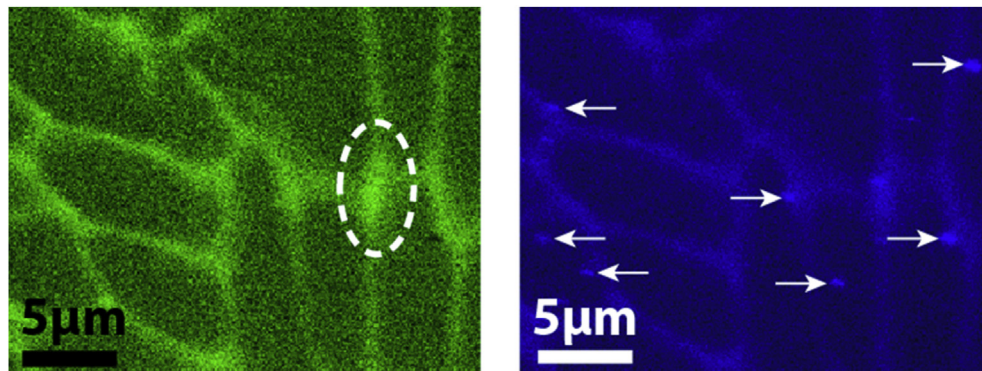

Fig. 3. EDS mappings from layer number 4 containing approximately 10 at% Al performed in the SEM showing Ni and Al enrichment at the dendrite boundaries. The Al rich dots observed in the Al map (marked by white arrows) were identified as Aluminum oxide particles. For both, Ni and Al, the Kα line was used for collecting the map signals.
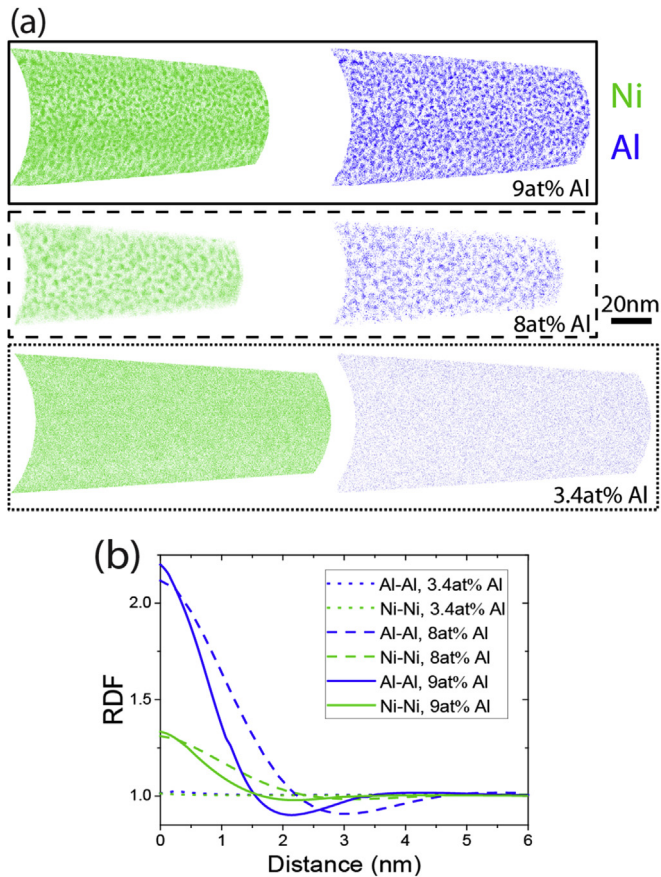
Fig. 4. (a) Atom maps of the solute atoms Ni and Al showing 100% of the atoms in a 6 nm thick slice through APT datasets obtained at different Al concentrations: bottom to top: 3.4, 8 and 9 at% respectively. (b) Corresponding concentration normalized RDFs: 3.4 at% Al dotted lines, 8 at% Al dashed lines and 9 at% Al solid lines. At a nominal Al content of 3.4 at% no clustering occurs. Higher content leads to clear cluster indication.

APT measurements were conducted at three different Al concentrations (i.e. taken from three different layers of the graded sample). The results are shown in Fig. 4. Fig. 4(a) depicts atom maps of both solute atoms, Ni and Al, in a 6 nm thick slice through the APT dataset. At a comparatively low Al concentration of 3.4 at%, a homogeneous distribution of Ni and Al can be observed while at higher Al concentrations of 8 at% and 9 at%, clearly clustering of Ni and Al takes place. The Al content was obtained as the bulk concentration of the respective APT measurement, collected over the entire tip.

A more quantitative measure of clustering of solute elements is given in Fig. 4(b) in the form of a Radial Distribution Function (RDF). A bin width of 0.2 nm was used and the measured concentration at each point was normalized to the bulk concentration of that element, i.e. a RDF value of one at a given distance means that it is as likely to find an atom as would be expected from the average concentration of this type of atom. The RDFs confirm the conclusions from visual inspection of the atom maps: It can be seen that no clustering takes place at a nominal alloy content of 3.4 at% Al while Al-Al and Ni-Ni clustering occurs at 8 at% and 9 at% Al. Using the volume of the reconstruction of the APT tip, the number density of precipitates was calculated to be 5×10^{24} particles/m^3 and 1.2×10^{25} particles/m^3 for 8 and 9 at% Al, respectively. For each Al concentration at least 6 APT tips were measured that all showed approximately the same number density.

In addition to the upper bound for the Al concentration of 15 at% derived from the requirement to obtain a martensitic microstructure, it is now possible to establish a lower bound for the Al concentration of approximately 3−5 at%. Below this concentration, no precipitates are formed in the as-produced state by IHT.

Fig. 5 shows a more detailed analysis of an APT dataset containing 8 at% Al. Only one type of precipitates could be identified. These nanometer-sized, spherical precipitates are enriched in both Ni and Al and are shown by means of iso-concentration surfaces in Fig. 5(a). Based on these surfaces, a proximity histogram was calculated, Fig. 5(b). These precipitates are enriched to approximately 35−45 at% in Ni and 35 at% in Al. Additionally, they contain a high amount of Fe of approximately 15−30 at%. The matrix is rather depleted in Al but still contains rather large amounts of Ni. The composition obtained experimentally does not fit to either that of NiAl nor Ni$_3$Al, the two prevalent precipitate phases reported in literature for similar alloys. This fact is illustrated by the two vertical, blue lines in the proximity histogram of Fig. 5(b) showing the expected Al concentration for both phases. It is known from literature that there is some solubility of Fe in NiAl [21,22,25,54−56]. Whether Fe occupies the Ni or the Al sublattice sites in NiAl is not straightforward and seems to depend on the Al concentration [57]. According to Yang et al. [58], Fe occupies the Al sites. Even if it is assumed that Fe substitutes Al, the ratio of (Al+Fe)/Ni is around 1.5 instead of 1 as would be expected for stoichiometric Ni(Al,Fe).

It was therefore not possible to decide unambiguously which type of precipitate was present in the material from the chemical information obtained from APT. In addition to a different composition, the two precipitate phases also show a different crystal structure, namely B2 (NiAl) and L1$_2$ (Ni$_3$Al) [24,28,58−62]. Fig. 6(a) and (b) show a representative 2-θ range for HEXRD spectra acquired at Al contents of 10 at% and 20 at% i.e. from the coarse
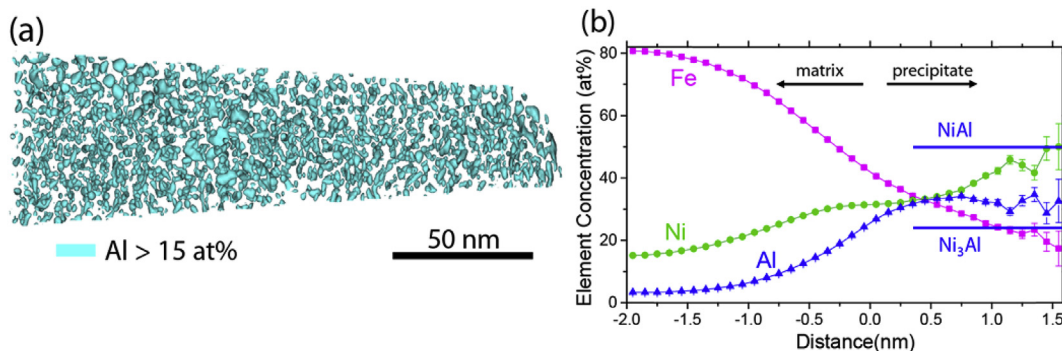

Fig. 5. (a). Precipitates visualized by drawing an isoconcentration surface at 15 at% Al. (b) Corresponding proximity histogram plotting the chemical composition as a function of the distance to the isoconcentration surface. Expected Al concentrations for NiAl and Ni$_3$Al are shown.
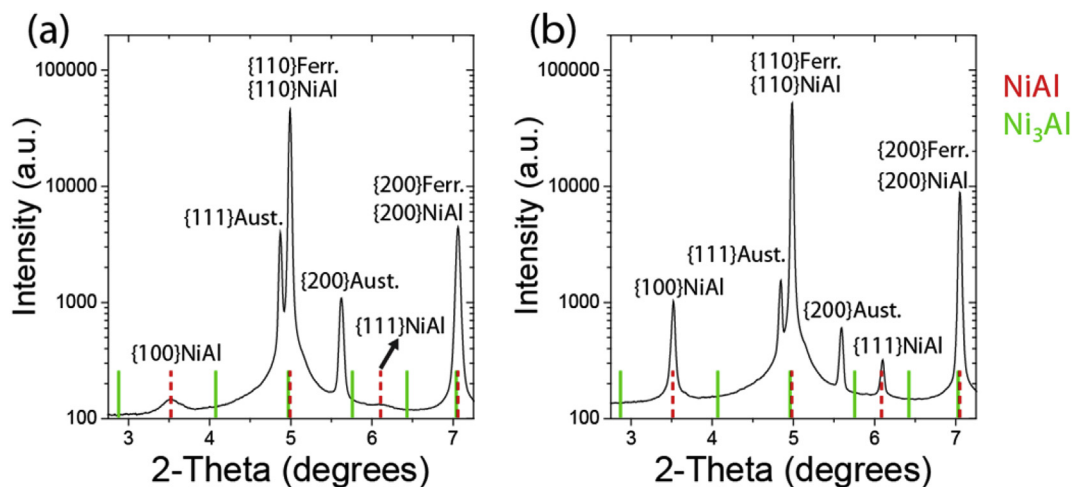
Fig. 6. Representative 2-θ range of XRD spectra from a layer containing (a) 10 at% Al and (b) 20 at% Al. The expected peak positions for NiAl and Ni₃Al are indicated by red, dashed lines and solid green lines, respectively. All peaks present in the HEXRD spectra are labeled with the corresponding lattice plane families (martensite being represented by ferrite). (For interpretation of the references to colour in this figure legend, the reader is referred to the web version of this article.)

Table 1
Phase volume fractions and lattice parameters for martensite/ferrite, austenite and NiAl obtained from Rietveld analysis of the HEXRD patterns at 10 and 20 at% Al concentrations.

Al content	Martensite/ferrite phase fraction/lattice parameter	Austenite phase fraction/lattice parameter	NiAl phase fraction/lattice parameter
10 at%	85 vol%	9 vol%	6 vol%
	2.8720 Å	3.6264 Å	2.8688 Å
20 at%	81 vol%	4 vol%	15 vol%
	2.8750 Å	3.6264 Å	2.8817 Å

grained ferritic and fine grained martensitic microstructures respectively. The expected peak positions for NiAl and Ni₃Al are indicated in the figure. Note that the martensitic matrix is cubic and hence indexed by peaks pertaining to ferrite. It is evident that the precipitate phase is NiAl. The spectra do not show any peak associated with L1₂ (Ni₃Al). The peaks at 3.51° and 6.09° perfectly fit to NiAl and cannot be produced by any other phase that occurs in the sample. In addition to the martensitic matrix and NiAl, austenite was found to be present.

The results of the Rietveld analysis, i.e. the phase volume fractions as well as the lattice parameters for martensite, austenite and NiAl, are shown in Table 1. The entire 2-θ range acquired (2−20°) was used for the Rietveld analysis. The martensitic microstructure contains 6 vol% of NiAl precipitates and 9 vol% Austenite.

4. Discussion

The HEXRD measurements reveal that the nanometer sized precipitates are structured B2 NiAl particles. The fact that the ratio of (Al+Fe)/Ni as measured by APT is not 1, as mentioned above, can partially be attributed to trajectory aberrations [40] due to different evaporation fields of the intermetallic precipitates NiAl and the matrix [63]. From the proximity histogram shown in Fig. 5(b) we observe that inside the precipitates the Al content is around 10 at% lower than the Ni content, which suggests that some Al sites are occupied by Fe atoms. The precipitate phase can therefore be written as Ni(Al,Fe) with Fe being approximately 10 at%. Nevertheless, the proximity histogram shows a higher Fe content inside the precipitate of approximately 15−25 at%. This allows to roughly estimate the effect of Fe atoms from the matrix being projected into the precipitate due to the above mentioned trajectory aberrations to approximately account for the remaining 10−15 at%.

The lattice mismatch between the NiAl precipitate phase and the surrounding martensitic microstructure was calculated from the lattice constants obtained from the Rietveld analysis (Table 1) to be 0.11%. This low lattice mismatch results in a likewise low coherency strain between nucleus and matrix, which in turn is associated with a low nucleation barrier and hence, high nucleation rate [64]. This fact can explain the exceptionally high precipitate density of up to 1.2×10^{25} m^{-3} found in the current alloy.

Hardness measurements along the varying Al concentration of the martensitic region of the graded sample were performed to identify influence of the high number density of the nanometer sized precipitates on the mechanical properties. The mean hardness value out of 10 individual measurements is shown for each layer of the graded sample up to the transition to the coarse ferrite grains in Fig. 7. The conversion from "layer number" to Al content was obtained using the Al concentration for each layer from the SEM-EDS scans as shown in Fig. 1(a). The hardness increases from 300 HV at 0 at% Al up to 525 HV at 12 at%. The microstructure at 0 at% Al consists of the same cellular/dendritic microstructure (with Ni enrichment at interdendritic regions) as the higher-Al layers, but does not contain any precipitates. The steep increase in hardness with increasing Al content is therefore directly associated with the precipitation of the high number density of nanometer sized NiAl particles as well as a reduced contribution from solid-solution strengthening.

Depositing graded samples by LMD presents an efficient way of screening a large variety of alloy compositions. However, in such an experiment, always two parameters, namely the IHT and the alloy composition, are varied at the same time from layer to layer. The further downward (i.e. closer to the substrate) a certain layer lies within a sample, the more layers were deposited on top and thus the more IHT the layer has experienced. In other words, the bottom
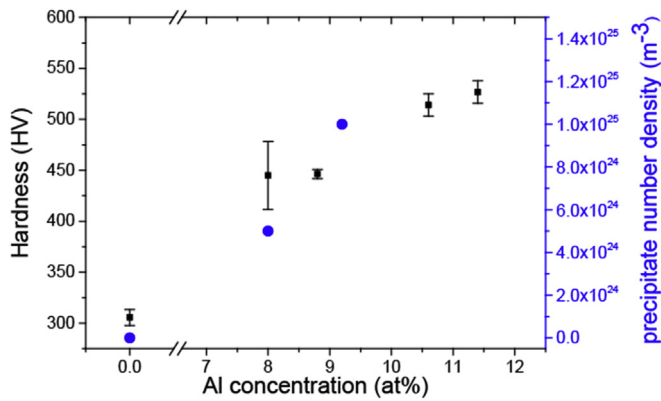
Fig. 7. Vickers hardness measurements along the layers of the martensitic region of the graded sample along the build direction i.e. following the Al gradient. A steep increase in hardness is observed with increasing Al concentration. Additionally, the precipitate number density as obtained from APT measurements is plotted in the same graph for Al concentrations at which APT measurements were available.

layers receive more IHT cycles compared to the top layers of the same sample. This applies to the present study but does not influence the main conclusions: if the determining factor for precipitation was the difference in IHT and not the difference in Al concentration, one would expect to find more pronounced precipitation in the *lower* layers which received more IHT cycles. However, we observe the opposite, i.e. more pronounced precipitation in the *upper* layers of the martensitic region which received less IHT. The more pronounced precipitation in the upper layers can hence be assigned unambiguously to the higher Al concentration instead of a more pronounced IHT. This is attributed to the fact that the graded sample used in this study was built starting from a low Al concentration at the bottom layers to a high Al level in the top layers.

From the concentration on the left hand side of the proximity histogram in Fig. 5(b) it can be seen that only 3—4 at% Al are left in the matrix. A substantial amount of the total Al content of the alloy apparently has precipitated from the matrix. Since no subsequent heat treatment was applied after the LMD manufacturing process, the precipitation of the high number density of NiAl can be attributed to the IHT.

In most LAM-processes used to synthesize metallic materials, the dominating pathway of heat removal is conduction away from the position of heat input (i.e. the melt pool) to the substrate through the previously deposited layers. This means that all these LAM processes always include an IHT. The strength of the IHT is strongly dependent on the process parameters and on the type of LAM processes applied e.g. the specific IHT is typically stronger in LMD than in SLM [31]. Furthermore, the effect of the IHT on the material microstructure is obviously substantially different for different alloys [35,65].

In this study a combination of alloy and process parameters was established that results in a pronounced in-process precipitation strengthening. For different process-material combinations the effect of the IHT might be very different. Nevertheless, the IHT might play an important role in all heat treatable alloys used in LAM processes, for example Al-Sc(-Zr), and should always be taken into account when designing alloys and heat treatments for such alloys.

5. Conclusions

1. This study presents the successful development of a model maraging steel alloy consisting of Fe, Ni and Al, that shows a pronounced response to the intrinsic heat treatment (IHT) imposed during a Laser Additive Manufacturing (LAM) process. Without any further heat treatment, it was possible to produce a maraging steel that is intrinsically precipitation strengthened by an extremely high number density of 1.2×10^{25} m^{-3} NiAl nanoparticles of 2—4 nm size. The high number density is related to the low lattice mismatch between the martensitic matrix and the NiAl phase.

2. Using a compositionally graded specimen, a large region in composition space in an Fe-19Ni-xAl (at%) alloy with x ranging from 0 to roughly 25 at% was screened to identify promising compositional regions for further studies.

3. The upper bound of Al concentrations that yields the desired martensitic microstructure was identified to be approximately 15 at%. Above this concentration, a coarse grained ferritic microstructure was formed instead of the desired martensitic one. The lower compositional bound was determined to be roughly 3—5 at%. Below this concentration, no NiAl precipitates are formed by the IHT. Within the process window between the lower and upper bound, the hardness increased with increasing Al concentration.

4. Atom Probe Tomography was capable of quantifying the high number density of nanoparticles present in specific layers of the LAM sample. Using high energy X-ray diffraction, the crystal structure of the precipitate phase was confirmed to be B2 NiAl. Different from the expected NiAl stoichiometry the Al content was found to be lower than that of Ni and a significant amount of Fe was present in the precipitate. This was partly attributed to artifacts from the field evaporation process of APT and partly to Fe replacing some Al in the precipitate.

5. The pronounced effect of the IHT on the ternary Fe-Ni-Al model alloy as found in this study shows the opportunities for development of alloys that are specifically designed for LAM-processes exploiting the unique features of these processes such as the IHT.

References

[1] N. Guo, M.C. Leu, Additive manufacturing: technology, applications and research needs, Front. Mech. Eng. 8 (2013) 215—243, http://dx.doi.org/10.1007/s11465-013-0248-8.

[2] J. Mazumder, A. Schifferer, J. Choi, Direct materials deposition: designed macro and microstructure, Mater. Res. Innov. 3 (1999) 118—131, http://dx.doi.org/10.1007/s100190050137.

[3] A. Gasser, G. Backes, I. Kelbassa, A. Weisheit, K. Wissenbach, Laser additive manufacturing: laser metal deposition (LMD) and selective laser melting (SLM) in turbo-engine applications, Laser Mater. Process (2010) 58—63, http://dx.doi.org/10.1002/latj.201090029.

[4] G.K. Lewis, E. Schlienger, Practical considerations and capabilities for laser assisted direct metal deposition, Mater. Des. 21 (2000) 417—423, http://dx.doi.org/10.1016/S0261-3069(99)00078-3.

[5] L. Qian, J. Mei, J. Liang, X. Wu, Influence of position and laser power on thermal history and microstructure of direct laser fabricated Ti—6Al—4V samples, Mater. Sci. Technol. 21 (2005) 597—605, http://dx.doi.org/10.1179/174328405X21003.

[6] B. Zheng, Y. Zhou, J.E. Smugeresky, J.M. Schoenung, E.J. Lavernia, Thermal behavior and microstructure evolution during laser deposition with laser-engineered net shaping: Part II. Experimental investigation and discussion, Metall. Mater. Trans. A Phys. Metall. Mater. Sci. 39 (2008) 2237—2245, http://

dx.doi.org/10.1007/s11661-008-9566-6.

[7] W. Hofmeister, M. Griffith, M. Ensz, J. Smugeresky, Solidification in direct metal deposition by LENS processing, Jom 53 (2001) 30–34, http://dx.doi.org/10.1007/s11837-001-0066-z.

[8] B. Zheng, Y. Zhou, J.E. Smugeresky, J.M. Schoenung, E.J. Lavernia, Thermal behavior and microstructural evolution during laser deposition with laser-engineered net shaping: Part I. Numerical calculations, Metall. Mater. Trans. A Phys. Metall. Mater. Sci. 39 (2008) 2228–2236, http://dx.doi.org/10.1007/s11661-008-9557-7.

[9] M.L. Griffith, M.E. Schlienger, L.D. Harwell, M.S. Oliver, M.D. Baldwin, M.T. Ensz, M. Essien, J. Brooks, C.V. Robino, J.E. Smugeresky, W.H. Hofmeister, M.J. Wert, D.V. Nelson, Understanding thermal behavior in the LENS process, Mater. Des. 20 (1999) 107–113, http://dx.doi.org/10.1016/S0261-3069(99)00016-3.

[10] Y. Zhang, G. Yu, X. He, Numerical study of thermal history in laser aided direct metal deposition process, Sci. China Phys. Mech. Astron. 55 (2012) 1431–1438, http://dx.doi.org/10.1007/s11433-012-4793-7.

[11] V.K. Balla, P.D. DeVasConCellos, W. Xue, S. Bose, A. Bandyopadhyay, Fabrication of compositionally and structurally graded Ti-TiO2 structures using laser engineered net shaping (LENS), Acta Biomater. 5 (2009) 1831–1837, http://dx.doi.org/10.1016/j.actbio.2009.01.011.

[12] R.M. Mahamood, E. Akinlabi, Lasermetal deposition of functionally graded Ti6Al4V/TiC, Mater. Des. 84 (2015) 402–410.

[13] H. Knoll, S. Ocylok, A. Weisheit, H. Springer, E. Jägle, D. Raabe, Combinatorial alloy design by laser additive manufacturing, Steel Res. Int. 87 (2016) 1–11, http://dx.doi.org/10.1002/srin.201600416.

[14] W. Sha, Z. Guo, Maraging Steels: Modelling of Microstructure, Properties and Applications, CRC Press, New York, 2009, http://dx.doi.org/10.1533/9781845696931.142.

[15] R.F. Decker, J.T. Eash, A.J. Goldman, 18% Nickel maraging steel, Trans. ASM 55 (1962) 58–76.

[16] R.F. Decker, Source Book on Maraging Steels, American Society for Metals International, Metals Park, OH, 1979.

[17] D. Raabe, D. Ponge, O. Dmitrieva, B. Sander, Designing ultrahigh strength steels with good ductility by combining transformation induced plasticity and martensite aging, Adv. Eng. Mater 11 (2009) 547–555, http://dx.doi.org/10.1002/adem.200900061.

[18] E.V. Pereloma, A. Shekhter, M.K. Miller, S.P. Ringer, Ageing behaviour of an Fe-20Ni-1.8Mn-1.6Ti-0.59Al (wt%) maraging alloy: clustering, precipitation and hardening, Acta Mater. 52 (2004) 5589–5602, http://dx.doi.org/10.1016/j.actamat.2004.08.018.

[19] T.V. Philip, T.J. McCaffrey, Ultrahigh strength steels, in: G.T. Murray (Ed.), Handb. Mater. Sel. Eng. Appl, CRC Press, New York, 1997, pp. 149–162.

[20] M.N. Rao, Progress in understanding the metallurgy of 18% nickel maraging steels, Int. J. Mater. Res. 97 (2006) 1594–1607.

[21] R. Schnitzer, R. Radis, M. Nöhrer, M. Schober, R. Hochfellner, S. Zinner, E. Povoden-Karadeniz, E. Kozeschnik, H. Leitner, Reverted austenite in PH 13-8 Mo maraging steels, Mater. Chem. Phys. 122 (2010) 138–145, http://dx.doi.org/10.1016/j.matchemphys.2010.02.058.

[22] Z. Guo, W. Sha, D. Vaumousse, Microstructural evolution in a PH13-8 stainless steel after ageing, Acta Mater. 51 (2003) 101–116, http://dx.doi.org/10.1016/S1359-6454(02)00353-1.

[23] D.H. Ping, M. Ohnuma, Y. Hirakawa, Y. Kadoya, K. Hono, Microstructure evolution in 13Cr-8Ni-2.5Mo-2Al martensitic precipitation-hardened stainless steel, Mater. Sci. Eng. A 394 (2005) 285–295, http://dx.doi.org/10.1016/j.msea.2004.12.002.

[24] S.D. Erlach, H. Leitner, M. Bischof, H. Clemens, F. Danoix, D. Lemarchand, I. Siller, Comparison of NiAl precipitation in a medium carbon secondary hardening steel and C-free PH13-8 maraging steel, Mater. Sci. Eng. A 429 (2006) 96–106, http://dx.doi.org/10.1016/j.msea.2006.05.071.

[25] R. Schnitzer, M. Schober, S. Zinner, H. Leitner, Effect of Cu on the evolution of precipitation in an Fe-Cr-Ni-Al-Ti maraging steel, Acta Mater. 58 (2010) 3733–3741, http://dx.doi.org/10.1016/j.actamat.2010.03.010.

[26] R. Taillard, A. Pineau, B.J. Thomas, The precipitation of the intermetallic compound NiAl in Fe-19wt.%Cr alloys, Mater. Sci. Eng. 54 (1982) 209–219, http://dx.doi.org/10.1016/0025-5416(82)90115-X.

[27] V. Seetharaman, M. Sundararaman, R. Krishnan, Precipitation hardening in a PH 13-8 Mo stainless steel, Mater. Sci. Eng. 47 (1981) 1–11, http://dx.doi.org/10.1016/0025-5416(81)90034-3.

[28] J. Shin, J. Jeong, J. Lee, Microstructural evolution and the variation of tensile behavior after aging heat treatment of precipitation hardened martensitic steel, Mater. Charact. 99 (2015) 230–237, http://dx.doi.org/10.1016/j.matchar.2014.11.024.

[29] E.V. Pereloma, R.A. Stohr, M.K. Miller, S.P. Ringer, Observation of precipitation evolution in Fe-Ni-Mn-Ti-Al maraging steel by atom probe tomography, Metall. Mater. Trans. A Phys. Metall. Mater. Sci. 40 (2009) 3069–3075, http://dx.doi.org/10.1007/s11661-009-9993-z.

[30] S. Jiang, H. Wang, Y. Wu, X. Liu, H.- Chen, M. Yao, B. Gault, D. Ponge, D. Raabe, A. Hirata, M. Chen, Y. Wang, Z. Lu, Ultrastrong steel via minimal lattice misfit and high density nanoprecipitation, Nature (2017) in press.

[31] E.A. Jägle, Z. Sheng, P. Kürnsteiner, S. Oclok, A. Weisheit, D. Raabe, Comparison of maraging steel micro- and nanostructure produced conventionally and by Laser Additive Manufacturing, Materials 10 (2017) 8, http://dx.doi.org/10.3390/ma10010008.

[32] W. Xu, E.W. Lui, A. Pateras, M. Qian, M. Brandt, In situ tailoring microstructure

in additively manufactured Ti-6Al-4V for superior mechanical performance, Acta Mater. 125 (2017) 390–400, http://dx.doi.org/10.1016/j.actamat.2016.12.027.

[33] W. Xu, S. Sun, J. Elambasseril, Q. Liu, M. Brandt, M. Qian, Ti-6Al-4V additively manufactured by selective laser melting with superior mechanical properties, JOM 67 (2015) 668–673, http://dx.doi.org/10.1007/s11837-015-1297-8.

[34] J. Yang, H. Yu, J. Yin, M. Gao, Z. Wang, X. Zeng, Formation and control of martensite in Ti-6Al-4V alloy produced by selective laser melting, Mater. Des. 108 (2016) 308–318, http://dx.doi.org/10.1016/j.matdes.2016.06.117.

[35] Z. Wang, T.A. Palmer, A.M. Beese, Effect of processing parameters on microstructure and tensile properties of austenitic stainless steel 304L made by directed energy deposition additive manufacturing, Acta Mater. 110 (2016) 226–235, http://dx.doi.org/10.1016/j.actamat.2016.03.019.

[36] P. Krakhmalev, I. Yadroitsava, G. Fredriksson, I. Yadroitsev, In situ heat treatment in selective laser melted martensitic AISI 420 stainless steels, Mater. Des. 87 (2015) 380–385, http://dx.doi.org/10.1016/j.matdes.2015.08.045.

[37] E. Yasa, K. Kempen, J. Kruth, Microstructure and mechanical properties of Maraging Steel 300 after selective laser melting, in: Proc. 21st Int. Solid Free. Fabr. Symp, 2010, pp. 383–396.

[38] G. Casalino, S.L. Campanelli, N. Contuzzi, A.D. Ludovico, Experimental investigation and statistical optimisation of the selective laser melting process of a maraging steel, Opt. Laser Technol. 65 (2015) 151–158, http://dx.doi.org/10.1016/j.optlastec.2014.07.021.

[39] E.A. Jägle, P. Choi, J. Van Humbeeck, D. Raabe, Precipitation and austenite reversion behavior of a maraging steel produced by selective laser melting, J. Mater. Res. 29 (2014), http://dx.doi.org/10.1557/jmr.2014.204.

[40] B. Gault, M.P. Moody, J.M. Cairney, S.P. Ringer, Atom Probe Microscopy, Springer Verlag, New York, 2012.

[41] K. Hono, D. Raabe, S.P. Ringer, D.N. Seidman, Atom probe tomography of nanostructures, MRS Bull. 41 (2016) 23–29, http://dx.doi.org/10.1002/sia.5507.

[42] H. Leitner, R. Schnitzer, M. Schober, S. Zinner, Precipitate modification in PH13-8 Mo type maraging steel, Acta Mater. 59 (2011) 5012–5022, http://dx.doi.org/10.1016/j.actamat.2011.04.053.

[43] Y. Li, W. Yan, J.D. Cotton, G.J. Ryan, Y. Shen, W. Wang, Y. Shan, K. Yang, A new 1.9 GPa maraging stainless steel strengthened by multiple precipitating species, Mater. Des. 82 (2015) 56–63, http://dx.doi.org/10.1016/j.matdes.2015.05.042.

[44] T.L. Martin, A. Radecka, L. Sun, T. Simm, D. Dye, K. Perkins, B. Gault, M.P. Moody, P.A.J. Bagot, Insights into microstructural interfaces in aerospace alloys characterised by atom probe tomography, Mater. Sci. Technol. U.K. 32 (2016), http://dx.doi.org/10.1179/1743284715Y.0000000132.

[45] F. Moszner, S.S.A. Gerstl, P.J. Uggowitzer, J.F. Löffler, Structural and chemical characterization of the hardening phase in biodegradable Fe–Mn–Pd maraging steels, J. Mater. Res. 29 (2014) 1069–1076, http://dx.doi.org/10.1557/jmr.2014.84.

[46] D.J. Larson, T.J. Prosa, R.M. Ulfig, B.P. Geiser, T.F. Kelly, Local Electrode Atom Probe Tomography: a User's Guide, Springer, New York, 2013, http://dx.doi.org/10.1007/978-1-4614-8721-0.

[47] A.P. Hammersley, S.O. Svensson, M. Hanfland, A.N. Fitch, D. Häusermann, Two-Dimensional detector software: from real detector to idealised image or two-theta scan, High. Press. Res. 14 (1996) 235–248.

[48] A.P. Hammersley, S.O. Svensson, A. Thompson, H. Graafsma, Å. Kvick, J.P. Moy, Calibration and correction of distortions in two-dimensional detector systems, Nucl. Instrum. Methods Phys. Res. A 346 (1994) 312–321, http://dx.doi.org/10.1063/1.1145618.

[49] L. Lutterotti, Maud: Materials Analysis Using Diffraction, Version 2.0.

[50] K. Kempen, E. Yasa, L. Thijs, J.P. Kruth, J. Van Humbeeck, Microstructure and mechanical properties of selective laser melted 18Ni-300 steel, Phys. Procedia 12 (2011) 255–263, http://dx.doi.org/10.1016/j.phpro.2011.03.033.

[51] O. Dmitrieva, P. Choi, S.S.A. Gerstl, D. Ponge, D. Raabe, Pulsed-laser atom probe studies of a precipitation hardened maraging TRIP steel, Ultramicroscopy 111 (2011) 623–627, http://dx.doi.org/10.1016/j.ultramic.2010.12.007.

[52] O. Dmitrieva, D. Ponge, G. Inden, J. Millán, P. Choi, J. Sietsma, D. Raabe, Chemical gradients across phase boundaries between martensite and austenite in steel studied by atom probe tomography and simulation, Acta Mater. 59 (2011) 364–374, http://dx.doi.org/10.1016/j.actamat.2010.09.042.

[53] D. Raabe, M. Herbig, S. Sandlöbes, Y. Li, D. Tytko, M. Kuzmina, D. Ponge, P.P. Choi, Grain boundary segregation engineering in metallic alloys: a pathway to the design of interfaces, Curr. Opin. Solid State Mater. Sci. 18 (2014) 253–261, http://dx.doi.org/10.1016/j.cossms.2014.06.002.

[54] M.K. Miller, M.G. Hetherington, Atom probe analysis of β' precipitation in a model iron-based Fe-Ni-Al-Mo superalloy, Le. J. Phys. Colloq. 50 (1989), http://dx.doi.org/10.1051/jphyscol:1989872. C8–425-C8-428.

[55] M. Schober, R. Schnitzer, H. Leitner, Precipitation evolution in a Ti-free and Ti-containing stainless maraging steel, Ultramicroscopy 109 (2009) 553–562, http://dx.doi.org/10.1016/j.ultramic.2008.10.016.

[56] H. Leitner, M. Schober, R. Schnitzer, Splitting phenomenon in the precipitation evolution in an Fe-Ni-Al-Ti-Cr stainless steel, Acta Mater. 58 (2010) 1261–1269, http://dx.doi.org/10.1016/j.actamat.2009.10.030.

[57] O.N.C. Uwakweh, C.T. Liu, Mössbauer effect measurement evidence for magnetic transition in ordered Fe-doped NiAl, Intermetallics 15 (2007) 98–102, http://dx.doi.org/10.1016/j.intermet.2006.03.008.

[58] L. Yang, X.-L. Wang, C.T. Liu, J.A. Fernandez-Baca, C.L. Fu, J.W. Richardson,

D. Shi, Neutron diffraction study of the structure and low-temperature phase transformation in ternary NiAl+M (M=Ni,Fe,Co) alloys, Scr. Mater. 56 (2007) 911–914, http://dx.doi.org/10.1016/j.scriptamat.2006.12.043.

[59] G. Chen, X. Ni, T. Nsongo, Lattice parameter dependence on long-range ordered degree during order-disorder transformation, Intermetallics 12 (2004) 733–739, http://dx.doi.org/10.1016/j.intermet.2004.02.013.

[60] J.A. Wollmershauser, S. Kabra, S.R. Agnew, In situ neutron diffraction study of the plastic deformation mechanisms of B2 ordered intermetallic alloys: NiAl, CuZn, and CeAg, Acta Mater. 57 (2009) 213–223, http://dx.doi.org/10.1016/j.actamat.2008.08.066.

[61] Y. Mishin, M.J. Mehl, D.A. Papaconstantopoulos, Embedded-atom potential for B2-NiAl, Phys. Rev. B 65 (2002) 224114, http://dx.doi.org/10.1103/PhysRevB.65.224114.

[62] S. Höring, N. Wanderka, J. Banhart, The influence of Cu addition on precipitation in Fe-Cr-Ni-Al-(Cu) model alloys,, Ultramicroscopy 109 (2009) 574–579, http://dx.doi.org/10.1016/j.ultramic.2008.11.006.

[63] F. Vurpillot, A. Bostel, D. Blavette, Trajectory overlaps and local magnification in three-dimensional atom probe, Appl. Phys. Lett. 76 (2000) 3127, http://dx.doi.org/10.1063/1.126545.

[64] D.A. Porter, K.E. Eastering, Phase Transformation in Metals and Alloys, Springer-Science+Business Media, 1992.

[65] J.T. Bono, J.N. DuPont, D. Jain, S. Baik, D.N. Seidman, Investigation of strength recovery in welds of NUCu-140 steel through multipass welding and isothermal post-weld heat treatments, Metall. Mater. Trans. A (2015), http://dx.doi.org/10.1007/s11661-015-3087-x.